AGU PUBLICATIONS

JGR

Journal of Geophysical Research: Solid Earth

RESEARCH ARTICLE

10.1002/2014JB011719

Key Points:
- Postseismic effect on repeating earthquakes from the M7.6 Chi-Chi main shock
- A distinct behavior of waveform changes appears on both sides of the fault
- We discriminate the effect of surface damage from fault zone damage

Supporting Information:
- Figures S1–S4 and Texts S1–S4

Correspondence to:
K. H. Chen,
katepili@gmail.com

Citation:
Chen, K. H., T. Furumura, and J. Rubinstein (2015), Near-surface versus fault zone damage following the 1999 Chi-Chi earthquake: Observation and simulation of repeating earthquakes, *J. Geophys. Res. Solid Earth*, *120*, 2426–2445, doi:10.1002/2014JB011719.

Received 24 OCT 2014
Accepted 25 FEB 2015
Accepted article online 2 MAR 2015
Published online 6 APR 2015

Near-surface versus fault zone damage following the 1999 Chi-Chi earthquake: Observation and simulation of repeating earthquakes

Kate Huihsuan Chen[1], Takashi Furumura[2], and Justin Rubinstein[3]

[1]Department of Earth Sciences, National Taiwan Normal University, Taipei, Taiwan, [2]Earthquake Research Institute, University of Tokyo, Tokyo, Japan, [3]United States Geological Survey, Menlo Park, California, USA

Abstract We observe crustal damage and its subsequent recovery caused by the 1999 *M*7.6 Chi-Chi earthquake in central Taiwan. Analysis of repeating earthquakes in Hualien region, ~70 km east of the Chi-Chi earthquake, shows a remarkable change in wave propagation beginning in the year 2000, revealing damage within the fault zone and distributed across the near surface. We use moving window cross correlation to identify a dramatic decrease in the waveform similarity and delays in the *S* wave coda. The maximum delay is up to 59 ms, corresponding to a 7.6% velocity decrease averaged over the wave propagation path. The waveform changes on either side of the fault are distinct. They occur in different parts of the waveforms, affect different frequencies, and the size of the velocity reductions is different. Using a finite difference method, we simulate the effect of postseismic changes in the wavefield by introducing *S* wave velocity anomaly in the fault zone and near the surface. The models that best fit the observations point to pervasive damage in the near surface and deep, along-fault damage at the time of the Chi-Chi earthquake. The footwall stations show the combined effect of near-surface and the fault zone damage, where the velocity reduction (2–7%) is twofold to threefold greater than the fault zone damage observed in the hanging wall stations. The physical models obtained here allow us to monitor the temporal evolution and recovering process of the Chi-Chi fault zone damage.

1. Introduction

The M_w 7.6 Chi-Chi earthquake occurred on 21 September 1999 and is the most damaging earthquake to strike the Taiwan urban area over the past two decades. Over 2300 fatalities and 8700 injuries [*Ma et al.*, 1999] were attributed to its effects. Previous studies have documented a dramatic change in the subsurface structure associated with the Chi-Chi earthquake rupture [e.g., *C. H. Chen et al.*, 2001; *Y. G. Chen et al.*, 2001; *Ji et al.*, 2001; *Loevenbruck et al.*, 2002; *Ma et al.*, 2001; *Zeng and Chen*, 2001; *Hsu et al.*, 2002]. The largest ground motions from the Chi-Chi earthquake were horizontal peak ground accelerations of approximately 1 g and occurred on the hanging wall side of the thrust Chelungpu Fault (Figure 1). The surface rupture extended over 100 km [*Lee et al.*, 2006], with maximum displacements of 9.1 m horizontally and 4.4 m vertically, were found at the northern end of the fault [*Yu et al.*, 2001]. The postseismic slip distribution at depth inferred from GPS data suggests a postseismic relaxation time of a few hundred days after the Chi-Chi earthquake [*Yu et al.*, 2001; *Hsu et al.*, 2002; *Loevenbruck et al.*, 2004], whereas the temporal and spatial characteristics of the Chi-Chi aftershock sequences imply an 8 to 14 years relaxation time [*Loevenbruck et al.*, 2004]. Such a difference between geodetic measurements and seismicity likely indicates that two distinct physical processes are responsible for recovery of strength in coseismic damage zones. Yet *Perfettini and Avouac* [2004] obtained a relaxation time of 8.5 years by reconciling the geodesy-derived afterslip and aftershock decay, which requires a rate-strengthening process taking place at shallow depth of faults (brittle creep). The processes that control the damage and subsequent healing of fault zone rocks across a range of depths have not been fully understood.

Observations of repeating earthquake sequences (RES) have been successfully used to document in situ measures of fault healing processes [e.g., *Vidale et al.*, 1994; *Marone et al.*, 1995; *Vidale and Li*, 2003; *Schaff and Beroza*, 2004; *Peng et al.*, 2005]. These sequences are characterized by short recurrence intervals (*Tr*) immediately after the main shock, with *Tr* increasing with time since the main shock [*Schaff et al.*, 1998; *Baisch and Bokelmann*, 2001; *Schaff and Beroza*, 2004]. RES have also been studied to give a detailed picture of temporal and spatial changes in a crustal setting associated with major earthquakes [e.g., *Rubinstein and*

©2015. American Geophysical Union. All Rights Reserved.

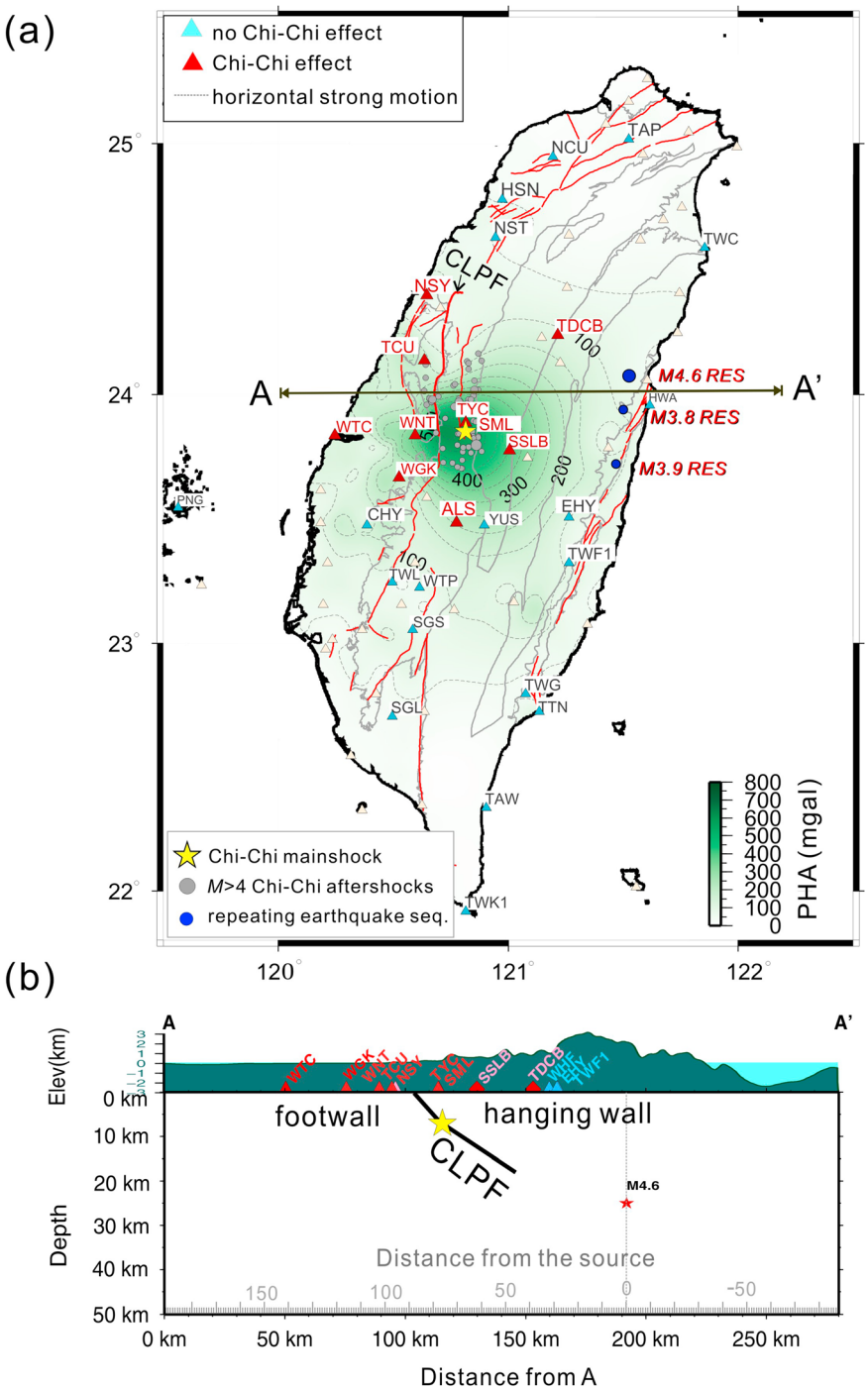

Figure 1. (a) Horizontal peak ground acceleration (PHA) map and spatial distribution of stations with the 1999 effect (red triangles) and no 1999 effect (blue triangles). Open triangles indicate the stations showing clipped or noisy seismograms, or lack of pre-1999/post-1999 events. Red lines indicate active faults in Taiwan. The Chi-Chi main shock and $M > 4$ aftershocks are denoted by yellow star and grey circles, respectively. Three quasi-periodic repeating earthquake sequences (RES) used in this study are indicated by blue circles. (b) Cross-section A-A′ showing the main rupture of the Chi-Chi earthquake sequence (black line) by *Kao and Chen* [2000] and spatial relationship with the *M*4.6 RES. The location of Chelungpu fault is indicated by CLPF. Yellow star indicates the *M*7.6 main shock. Red star indicates the M4.6 RES considered in the later finite difference simulation.

©2015. American Geophysical Union. All Rights Reserved.

Beroza, 2004; *Schaff and Beroza*, 2004; *Rubinstein and Beroza*, 2007; *Poupinet et al*., 1984; *Baisch and Bokelmann*, 2001]. For example, using the repeating events that occurred before and after the 1989 Loma Prieta *M*6.9 earthquake, *Baisch and Bokelmann* [2001] found that post-Loma Prieta events have reduced waveform similarity with pre-Loma Prieta events in the vicinity of the main shock epicenter, while other paths remain nearly unaffected. These changes gradually recover within 5 years after the main shock. *Rubinstein and Beroza* [2004] showed that the velocity change decreases coseismically, with the amplitude of the changes decaying logarithmically in time after the Loma Prieta main shock.

Earlier studies of the Chi-Chi earthquake have shown that the waveform characters of RES are changed by the 1999 *M*7.6 Chi-Chi earthquake [*Chen et al*., 2011]. The post-Chi-Chi events have reduced waveform similarity among RES compared with the pre-Chi-Chi events. The reduced waveform similarity is most pronounced at stations with large seismic intensities and close to large surface displacements (Figure 1a), suggesting that damage at the near surface may be responsible for the observed waveform changes. Given that the cross-correlation coefficient (ccc) changes are also significant at footwall sites where source-receiver paths propagate either along or across the rupture (Figure 1b), they inferred that the deep damage to the fault zone may have taken place, such that a combination of surface and fault zone damage contributed to the waveform changes observed following the Chi-Chi earthquake. Based on observations alone, it is difficult to pinpoint the location and magnitude of the velocity reductions that contributed to the measured waveform similarity change and time delays. Hence, a rigorous physical interpretation as to how and where the postseismic damage has been taking place, therefore, is lacking.

In this study we use finite difference methods (FDMs) to simulate wave propagation with the aim of separating the effects of fault zone damage from near-surface damage. The results allow us to estimate the physical size of these zones and the amount that the velocity was reduced. The physical models obtained here allow us to monitor the temporal evolution and recovering process of the fault zone damage, which have important implications for seismic hazard mitigation.

2. Observed Spatial Variation in Waveform Similarity and Time Lapse

We use the same data as *Chen et al*. [2011], which identified changes in waveform characteristics following the Chi-Chi earthquake. This data set consists of quasi-periodic *M*3.8–4.6 RES located ~70 km from the Chi-Chi earthquake (blue circles in Figure 1a). The RES were originally determined using 1991 to 2010 short-period seismic data from Central Weather Bureau Seismic Network (CWBSN) and 1996–2010 broadband seismic data from the Broadband Array in Taiwan for Seismology (BATS) with magnitude range of M_L 2.0 to 6.4. The seismograms processed were band pass filtered from 1 to 10 Hz and cut into a 30.5 s windows beginning 0.5 s before the *P* arrival. Those events having seismogram pairs with ccc greater than 0.70 were first selected as similar event pairs. The RES were then identified using composite selection approach that incorporates both waveform similarity (represented by ccc) and differential *S-P* (dS_mP) time information (at subsample precision) and allows effectively eliminating errors introduced by inaccurate origin times and interstation timing [*Chen et al*., 2008].

Using the $M > 3.5$ RES updated by *Chen et al*. [2011], we apply cross correlation in the frequency domain [*Poupinet et al*., 1984] with 1.2 s long windows, stepping forward at 1 s increments through 30 s after the *P* arrival (please see Figure S1 in the supporting information). Together with the waveform cross-correlation coefficient measurements, we find three major differences between post-Chi-Chi behavior in the hanging wall and footwall. These differences are most significant in the first post-Chi-Chi event for all RES considered.

First, the changes in waveform character (reduction in waveform similarity and travel time changes) occur in different portions of the seismogram for stations on different sides of the fault. Comparing the 1998 and 2001 events in the *M*4.6 RES, we found large reductions in waveform similarity (ccc < 0.7) appearing near/before the *S* wave arrival at footwall stations with travel paths crossing the rupture zone, as indicated by green color in the seismogram of Figure 2a. At hanging wall stations, however, similar reductions in waveform similarity are not found until the late *S* wave coda and surface waves. As shown in Figure 2b, large delays are also seen in the *P* coda or early *S* wave train at the footwall stations, while at hanging wall stations, large delays are seen in the late *S* coda. Delay time measurements become less reliable as ccc drops below 0.7. Therefore, in our quantitative assessment of delay times and velocity changes, we analyze the window starting at the *S* arrival until the time in the seismogram when ccc drops below 0.7.

©2015. American Geophysical Union. All Rights Reserved.

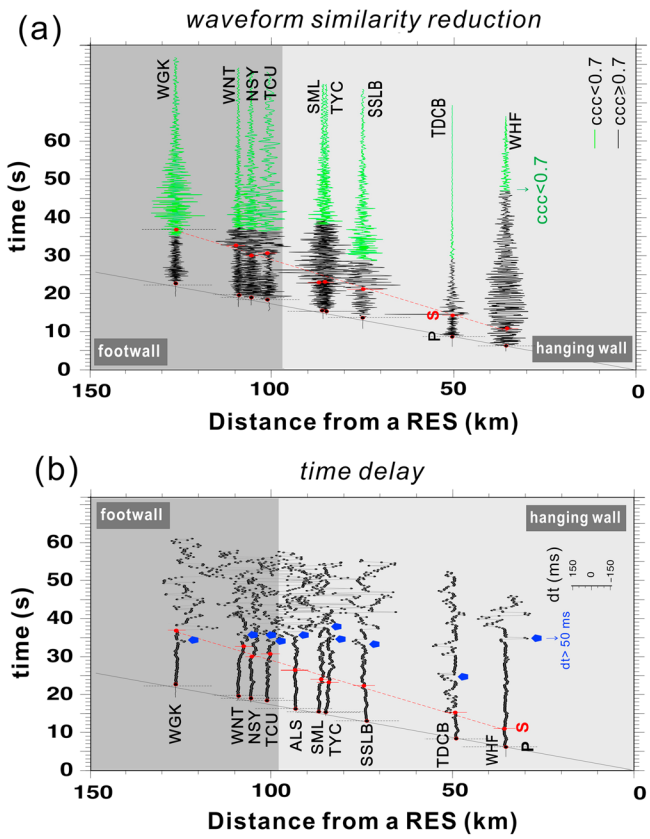

Figure 2. (a) Reduction in waveform similarity in the seismogram as a function of distance. We apply cross correlation in the frequency domain to obtain waveform cross-correlation coefficient and precise time lag between the pre- (17 May 1998) and post-1999 (26 July 2001) repeating events in the *M*4.6 RES. Red dot in the seismogram indicates *S* wave arrivals, whereas black dot indicates the *P* arrival. Major reduction in ccc (<0.7) is shown in green. (b) Delay time (d*t*) in the seismogram as a function of distance and time into the seismogram. The blue arrow indicates when d*t* exceeds 50 ms. Dark and light grey areas denote the footwall and hanging wall stations, respectively.

Second, we find that there is a difference in the frequency band in which a correlation coefficient reduction takes place. Using the same waveform data in Figure 2, the correlation coefficient reduction remains similar over much of the range of frequencies considered (2–6 Hz) and is smallest for the lowest frequencies (1 Hz) at the footwall stations (Figure 3a). At hanging wall stations, however, the most significant correlation coefficient reduction occurs for the highest frequencies considered (4–6 Hz) (Figure 3b).

Last, we have determined that the velocity change derived from delay time measurements is greater in the footwall stations than in the hanging wall stations. Figures 4a–4d illustrate how the regression line that represents velocity change is determined in a delay time as time plot. In Figure 4e, the 1998 and 2001 repeating events in the *M*4.6 RES illustrates the path-averaged velocity reduction ranging from 2.7 to 7.6% in the footwall stations (red symbols), larger than the <2% shear wave velocity change at hanging wall stations (black symbols). Two footwall stations NCU and CHY have very small velocity changes (<2%), which are likely due to the fact that they are far from the Chi-Chi source area. While the measurement is path averaged over the entire medium, we believe that the reduction is limited to a smaller area; hence, the velocity reductions in some areas are higher than the values shown in Figure 4.

3. Finite Difference Method Simulation

In order to understand what drives the different post-Chi-Chi behavior in hanging wall and footwall stations, we conduct a 2-D finite difference simulation and compare the synthetic seismograms and observations at footwall (fault zone crossing path) and hanging wall (nonfault zone crossing path) stations, to explain the cause of the above features in each area. As shown in Figure 5c, the 2-D model is taken along a profile across the Chi-Chi source area (A-A′ in Figure 1b), which covers a 204×78 km^2 area discretized with 25 m grid. The crust and upper mantle structural model in our model is from travel time topography by *Kim et al*. [2005] and a minimum shear wave velocity of V_s = 1.6 km/s (Figure 5c). Anelastic parameters for *P* and *S* waves are assumed as $Q_s = V_s/10$ and $Q_p = 2 \times Q_s$. Irregular surface topography is introduced in the simulation model based on the SRTM30_PLUS with a 30 arc sec resolution (roughly 1 km) digital elevation model [*Becker et al*., 2009].

The simulation generates high-frequency seismic wave propagation with maximum frequency of $f = 16$ Hz with a sampling of four grid points per minimum wavelength. A stochastic random heterogeneity model is also introduced in the velocity model, which is characterized by Von Karman distribution function with a horizontally elongated correlation distance of ax = 10 km, much shorter correlation distance in vertical

©2015. American Geophysical Union. All Rights Reserved.

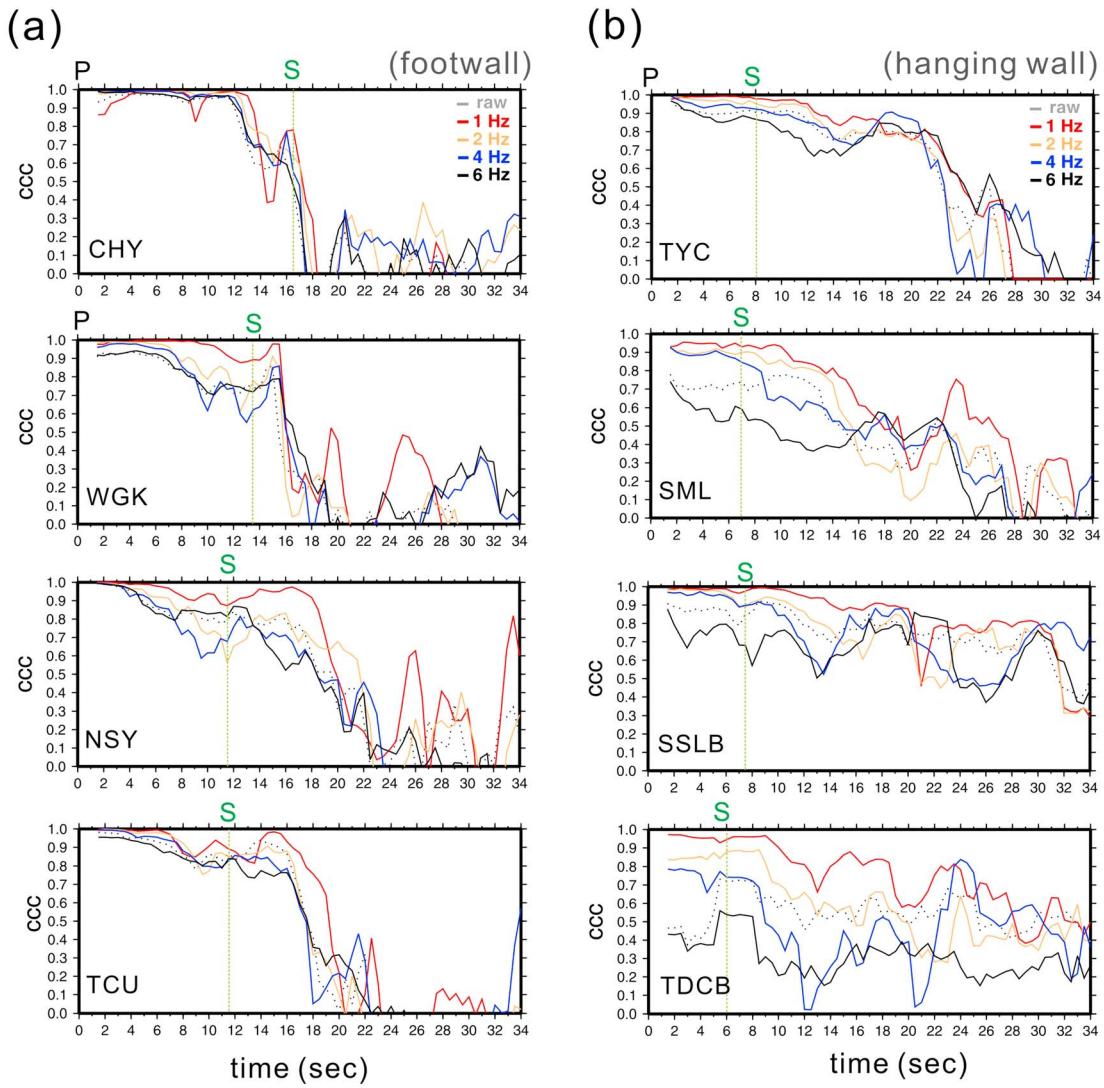

Figure 3. Reduction of waveform similarity (represented by ccc) as a function of time at different frequency bands between the pre- (17 May 1998) and post-1999 (26 July 2001) events in the *M*4.6 repeating sequence at (a) footwall stations and (b) hanging wall stations. Here we use 3 s long window, sliding forward at 0.5 s increments through 34 s after the *P* arrival in the computation.

direction (az = 0.5 km), and standard deviation of e = 2% for the crust and ax = 20 km, az = 1 km, and e = 2% in the mantle. The velocity deviation of the random heterogeneity is embedded over a background V_p and V_s model. Note that such small-scale heterogeneities are necessary to simulate realistic properties of the high-frequency ($f > 1$–2 Hz) scattering wavefield, though they are not reconstructed by the present tomography of relatively low resolution [e.g., *Kennett and Furumura*, 2008]. Artificial reflections from model boundaries are suppressed by applying perfectly matched layers absorbing boundary condition at 15 grid points surrounding the FDM model.

A double-couple source with a thrust faulting mechanism (strike = 63.1°, dip = 31.6°, and rake = 143.7) representing the reference *M*4.6 repeating event of 20 January 1994 is placed at the depth of 20.78 km (red star in Figure 1b). We use a Kupper-wavelet source-time function with maximum frequency of $f = 16$ Hz. The snapshot of wave propagation at time 12 s after the earthquake starts is shown in Figure 5d, where the *P* and *S* waves are shown in red and green, respectively, which is derived by calculating the divergence and rotation of the 2-D wavefield, respectively. The *P* and *S* waves propagate to the west in the crust and upper mantle. Amplification and reverberation in the near-surface sediments is also evident. We also produce the synthetic seismograms in radial (R) and vertical (Z) components, as shown

©2015. American Geophysical Union. All Rights Reserved.

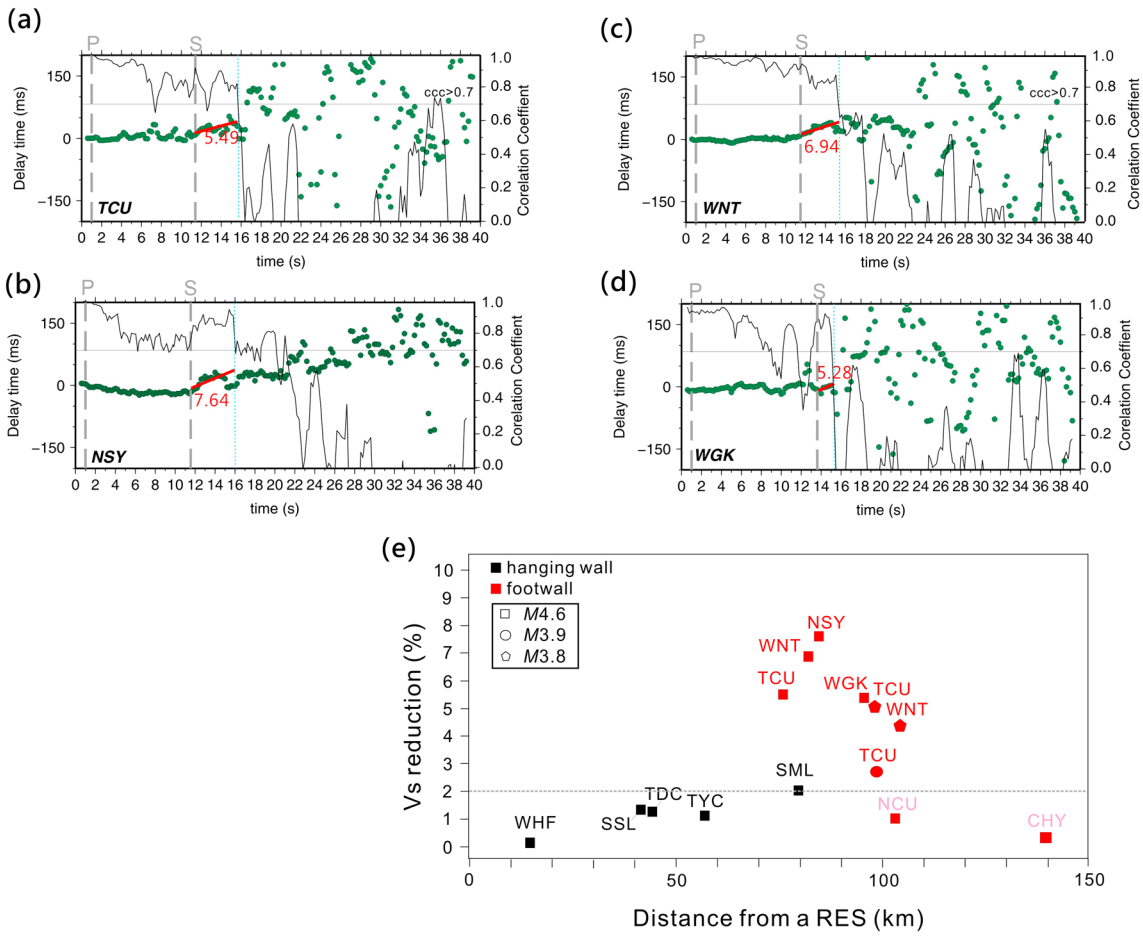

Figure 4. (a)–(d) Example of delay time (green dots scaled on the left axis) and waveform cross-correlation coefficient (black line scaled on the right axis) as a function of time at four stations showing relatively big *S* wave velocity reduction in Figure 4e. The delay time is calculated using event pair between a pre-Chi-Chi event on 17 May 1998 and a post-Chi-Chi event on 26 July 2001 in the *M*4.6 RES. The regression line that represents velocity change (red number) is determined at the time window starting from *S* arrival to the time when ccc drops below 0.7. The first and second vertical dashed lines indicate the *P* and *S* arrivals. (e) The observed velocity reduction as a function of epicenter-to-station distance from three different repeating sequences. Red and black symbols represent footwall and hanging wall stations, respectively.

in Figures 5a and 5b. Each seismogram is compensated for geometrical spreading (i.e., square root of the epicentral distance for the line source in 2-D wavefield) to increase the visibility of seismic signal at distant stations.

We first test whether source variability in the RES could produce our observations. We have tested the effect of different source locations, focal mechanisms, and source sizes and found that the observed spatial and temporal change in the ccc reduction is unlikely to be produced by such source effects (Figure S2 in the supporting information).

3.1. Change in Path Effect: Location of Low Velocity Anomaly

To test whether velocity changes can produce our observations we introduce low velocity anomalies (LVAs) in layers in the near surface and along the fault surface that produced the Chi-Chi earthquake. To best fit our observations we vary the location, thickness, and magnitude of the velocity reduction of the low velocity anomalies. At first, the LVA is assumed to have a thickness of 2 km with −4% V_s and −2% density change. To simplify the model, we assume that the *P* wave velocity (V_p) and anelastic parameters (Q_p, and Q_s) remain the same, given the fact that the V_p, Q_p, and Q_s anomaly in a thin layer have limited influence on the *S* wavefield.

Examples of seismic wavefield snapshot with the LVA on the surface (S-LVA) is shown in Figure 6a (left), which illustrates the spread of seismic *P* and *S* wave propagating in the crust and along the LVA. The S-LVA extended

©2015. American Geophysical Union. All Rights Reserved.

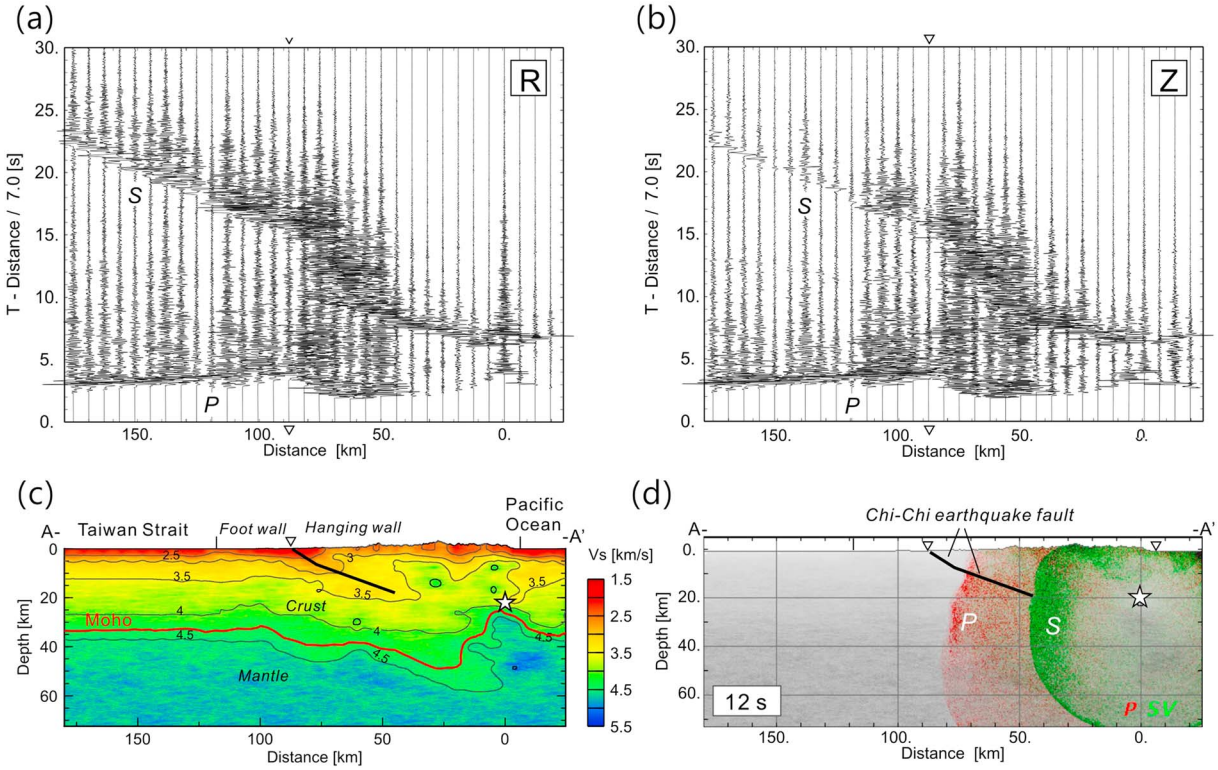

Figure 5. (a) Radial and (b) vertical components of synthetic seismograms. (c) Schematic of a 2-D fault model in the study area along the A-A′ profile in Figure 1b. Source as the repeatable *M*4.6 earthquake is denoted by open star. The velocity structure is based on 2-D tomography by *Kim et al.* [2005] with stochastic random heterogeneity introduced. Moho depth is chosen at $V_P = 7.5$ km/s [*Kuo-Chen et al.*, 2012], equivalent to $V_S = 4.3$ km/s, as denoted by red line. (d) Example of wavefield snapshot at 12 s. *P* and *S* waves are shown in red and green, respectively.

from the fault surface (reverse triangle in Figure 6a) to the western edge of Taiwan is indicated by the 30 km long open box. To find the change in the wavefield due to the LVA, we use the differential wavefield (Figure 6a, right) by subtracting the reference wavefield that has no velocity anomaly from the wavefield with S-LVA introduced. With the differential wavefield we can examine the spatiotemporal change in the simulated wavefield. Judging from the synthetic seismograms, we found a major change in wavefield on the footwall side through *P*-to-*P*, *P*-to-*S*, *S*-to-*P*, and *S*-to-*S* conversions at the boundary of the S-LVA. Such converted waves are mostly propagating to the west (i.e., the footwall side) of the S-LVA, with very little backscattering of the seismic waves to the east (i.e., hanging wall side). These converted waves arrive at footwall stations just after the *P* arrival and continue through the *S* wave coda. With a deep fault zone anomaly (F-LVA) in Figure 6b, we find significant changes in the wavefield on both sides of the fault as a result of seismic waves bouncing back and forth at the F-LVA boundary. This leads to *P*-to-*S*, *S*-to-*P*, and *S*-to-*S* conversions, whereas the *S*-to-*S* conversion along the F-LVA is strongest.

We further illustrate the effects on the arrival of ccc reduction in seismogram by considering both anomaly models. In Figure 7, the synthetic seismograms of the radial component ground motion of the LVA model is plotted, where the different levels of ccc reduction are highlighted by black, blue, and red for ccc > 0.7, ccc > 0.5, and ccc < 0.5, respectively. The maximum value in the differential wavefield from all snapshots is illustrated in the bottom panels of Figures 7a–7d, showing the distribution of the distorted wavefield in the cross section, where *P* and *S* wavefield is shown in red and green, respectively.

Figures 7a and 7b illustrate the effect of F-LVA, which is considered as two segments with a change in dip angle at 8 km depth [*Kao and Chen*, 2000]. From the snapshots and synthetic seismograms, we find that the major ccc reduction occurs only for limited number of hanging wall stations that are located right above the shallow F-LVA (Figure 7a), whereas the deeper F-LVA has broader influence at stations in the hanging wall and footwall sides (Figure 7b). Deeper F-LVA also produces late arrival of significant ccc change, as illustrated by red waveforms at hanging wall stations closer to the source (distance 50–80 km).

©2015. American Geophysical Union. All Rights Reserved.

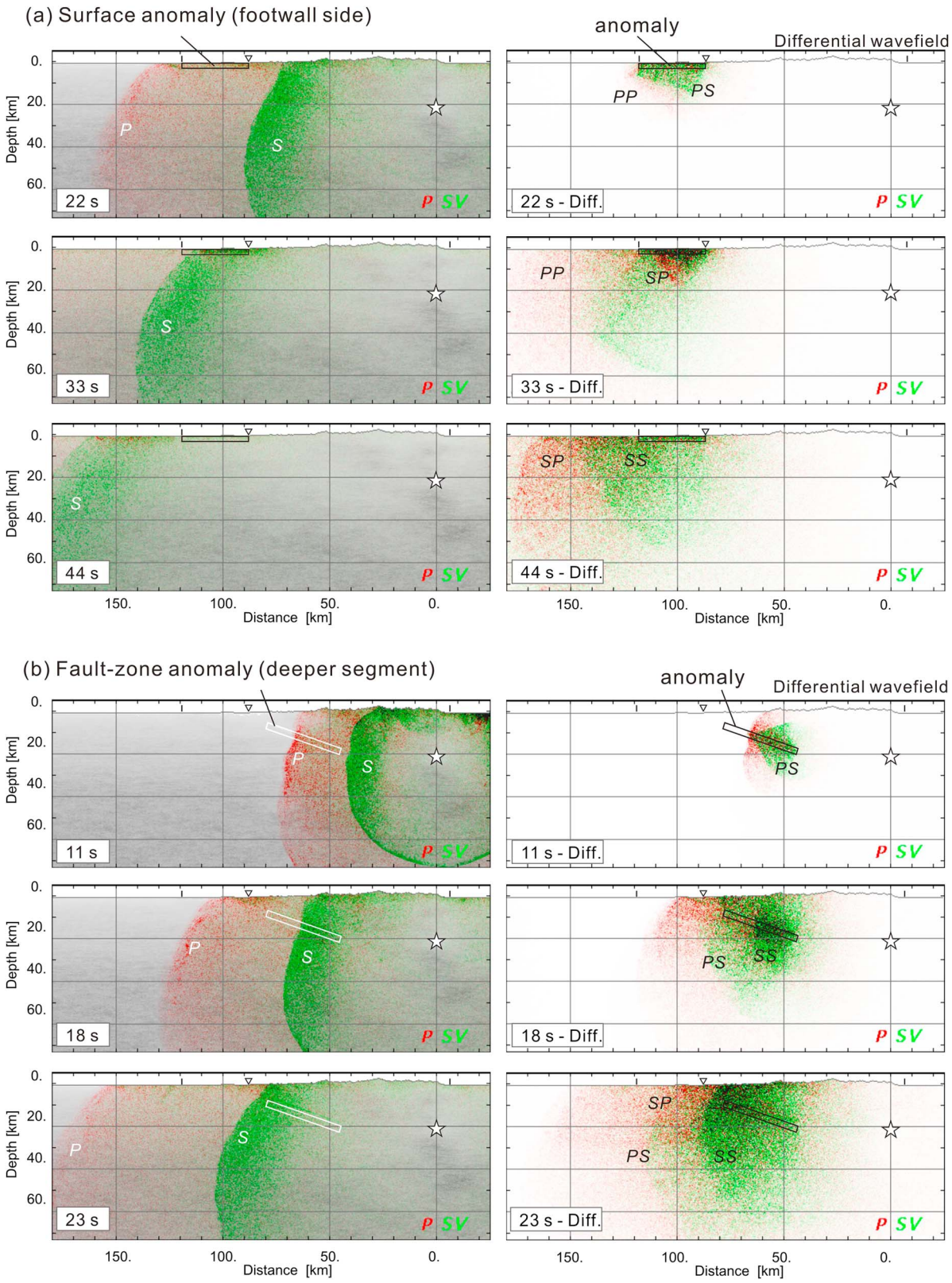

Figure 6. (a) Snapshots for reference wavefield (left) and differential wavefield (right), which is done by subtracting reference wavefield from wavefield with surface anomaly introduced (denoted by box). (b) Snapshots for reference wavefield (left) and differential wavefield (right), which is done by subtracting reference wavefield from wavefield with fault zone anomaly introduced (denoted by box). Reverse triangles indicate the location of fault trace in the cross section. *P* and *S* waves are shown in red and green, respectively.

©2015. American Geophysical Union. All Rights Reserved.

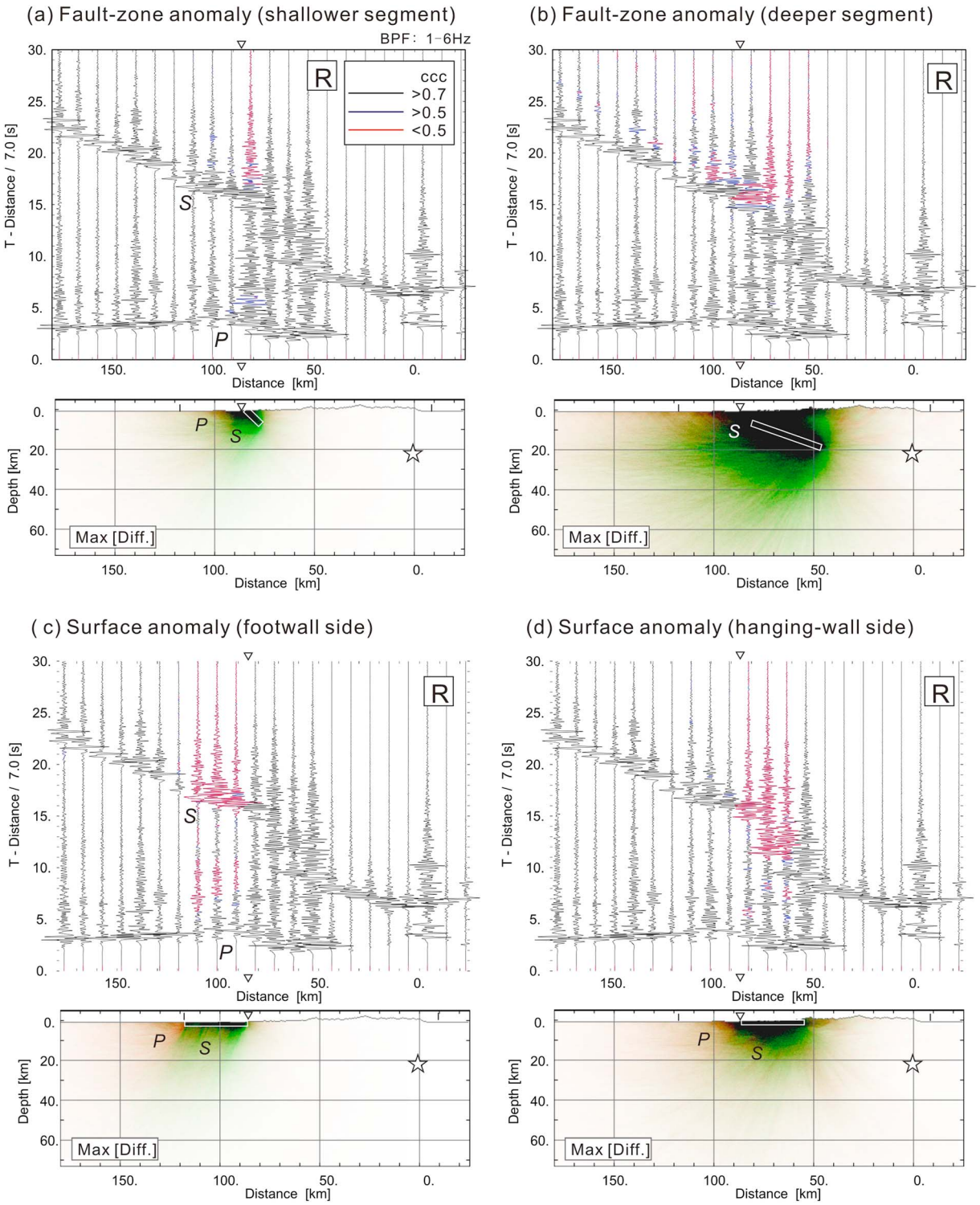

Figure 7. Simulated waveforms as a function of distance and maximum value of differential wavefield while introducing a 2 km low-velocity layer ($dV_p = 0\%$, $dV_s = -4\%$, and $dR_o = -2\%$) in deep fault zone and near surface. (a) Shallower fault zone LVA from surface to 8 km depth. (b) Deeper fault zone LVA from 8 km to 19 km depth. (c) Surface LVA in the footwall side. (d) Surface LVA in the hanging wall side. *P* and *S* wavefield is shown in red and green, respectively.

©2015. American Geophysical Union. All Rights Reserved.

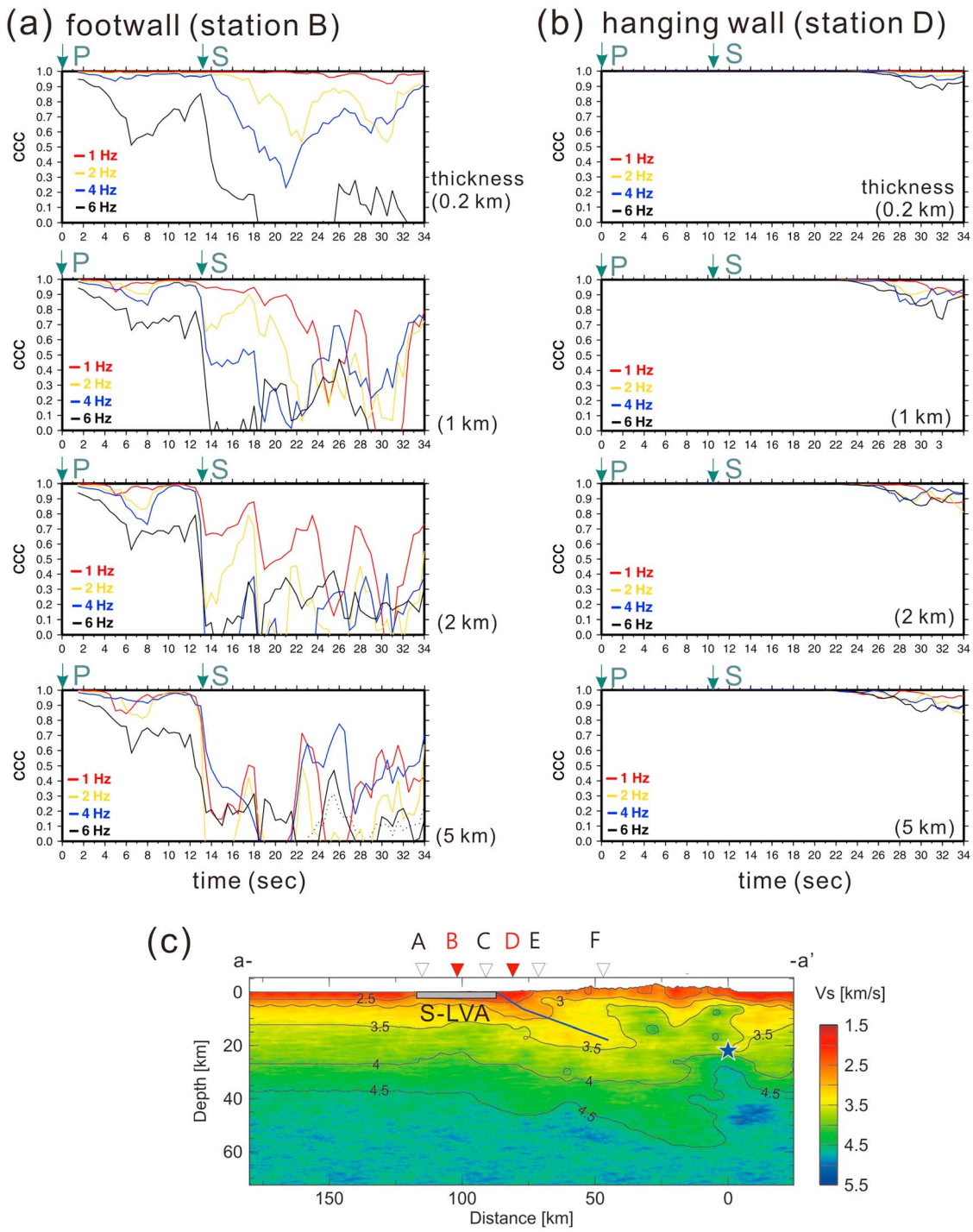

Figure 8. Surface LVA on the footwall side induced reduction in waveform similarity at different frequency bands at (a) footwall and (b) hanging wall stations. (c) Cross section showing location of target stations (stations B and D) and surface low velocity anomaly (grey area).

Figures 7c and 7d illustrate the effect of S-LVA. If the S-LVA is placed in the footwall, the ccc change is primarily in the early *P* coda and in the *S* and *S* coda (Figure 7c). Strong *P*-to-*S* and *S*-to-*P* conversions developing in the S-LVA below the surface appear to be responsible for these changes. If the S-LVA is placed on the hanging wall side, there is a ccc reduction in P coda that occurs at hanging wall stations close to the fault, and a ccc reduction in the early *S* coda at the hanging wall stations closest to the fault (Figure 7d). This is inconsistent with our observations, which shows late *S* coda ccc reductions (Figure 2) and minimal

©2015. American Geophysical Union. All Rights Reserved.

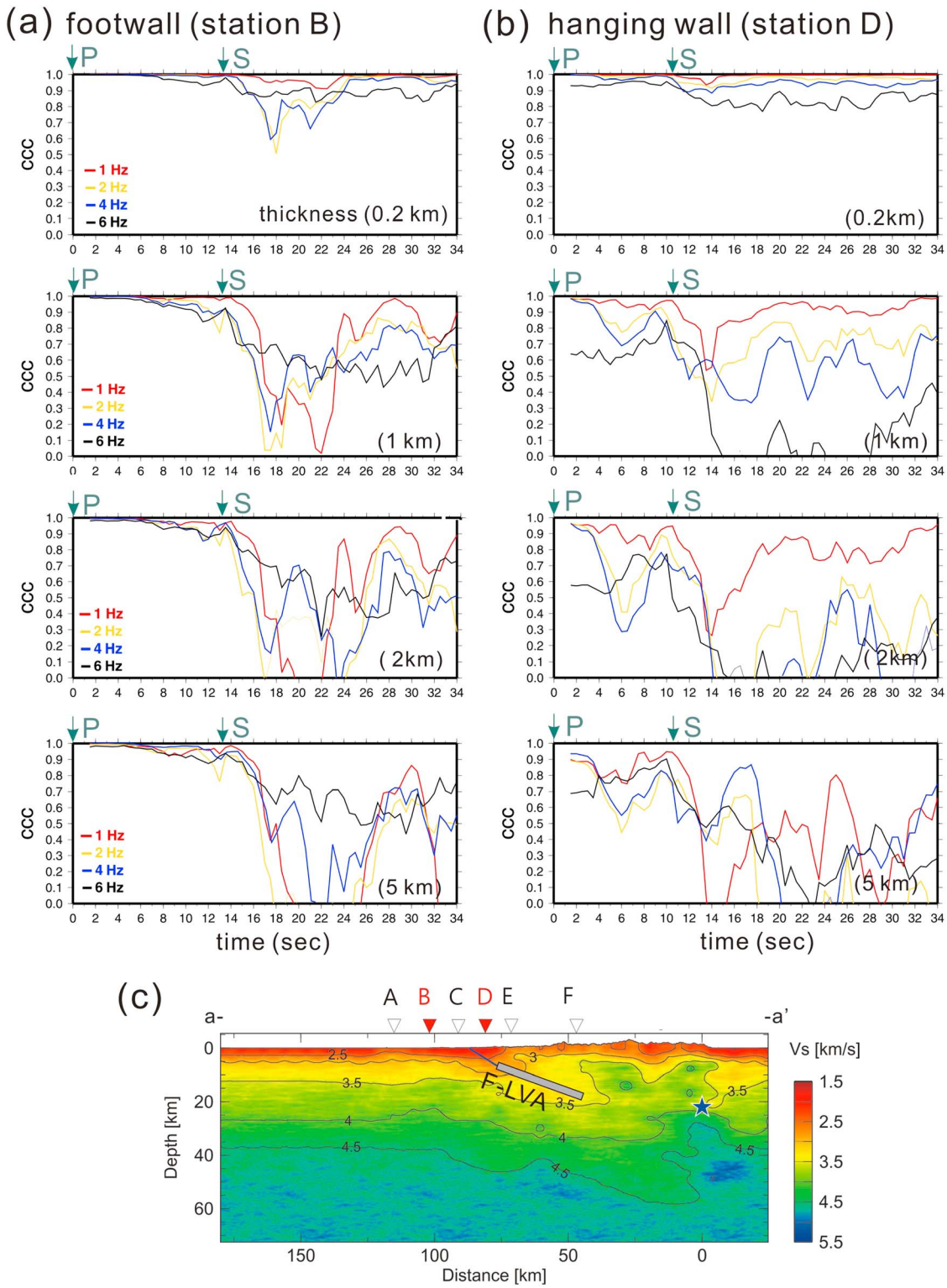

Figure 9. Deep fault zone LVA induced reduction in waveform similarity at different frequency bands at (a) footwall and (b) hanging wall stations. (c) Cross section showing location of target stations (stations B and D) and deep fault zone low velocity anomaly (grey area).

©2015. American Geophysical Union. All Rights Reserved.

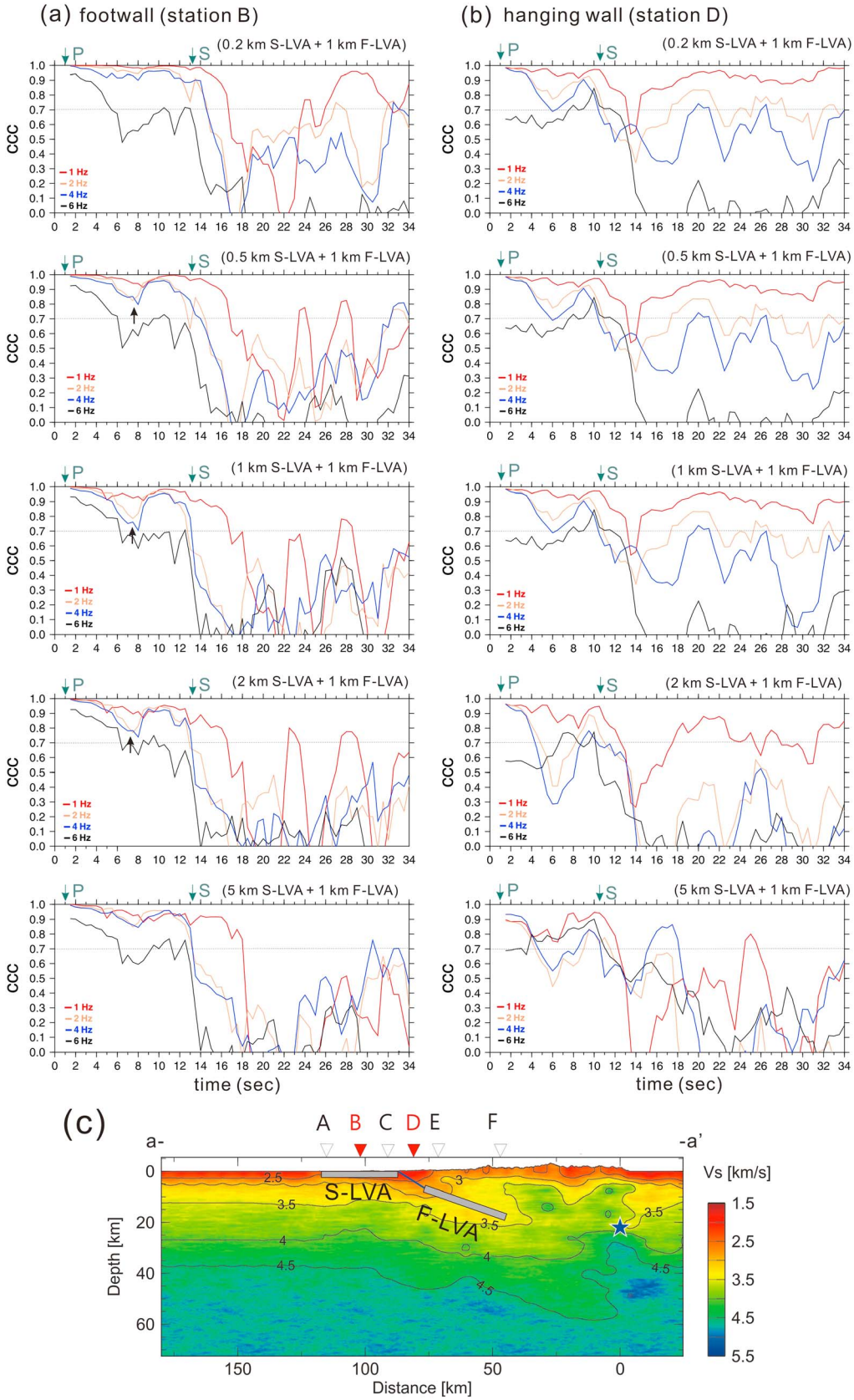

Figure 10

©2015. American Geophysical Union. All Rights Reserved.

P coda ccc reductions. Hence, we believe that hanging wall S-LVA does not contribute much or at all to the observed waveform changes.

Comparison between observations (Figure 2) and simulations (Figure 7) of the ccc reduction suggests a combination of pervasive damage near the surface on the footwall side of the fault and deep, along-fault damage. Shallow fault zone damage and shallow hanging wall damage are not necessary to reproduce our observations but cannot be ruled out either. The results suggest that the mechanism causing the reduction in ccc may be different for the footwall stations and the hanging wall stations. In the footwall stations, the observed ccc reduction starts in the *P* coda, which can be explained by footwall S-LVA in Figure 7c. In the hanging wall stations, the observed ccc reduction starts at later *S* coda for stations closer to the source, which is comparable to the differential wavefield generated by deep F-LVA in Figure 7d. The footwall S-LVA and deep F-LVA are therefore considered in the subsequent analysis.

3.2. Change in Path Effect: Thickness of Low Velocity Anomaly

We next examine how the thickness of the LVA influences the ccc reduction behavior in different frequency bands. A thinner LVA only affects a high-frequency wavefield characterized by wavelengths shorter than the thickness of the LVA, whereas a thicker LVA will influence a broader frequency band.

In Figure 8, we simulate the frequency dependence of the ccc reduction at a footwall station B (epicentral distance = 100 km) and hanging wall station D (epicentral distance = 75 km) using various thickness of S-LVA ranging from 0.2 km to 5 km with V_s reduction of −4% and density reduction of −2%. We plot the ccc change of the synthetic seismogram as a function of time for four frequency bands (center frequency = 1, 2, 4, and 6 Hz). In the footwall stations, the ccc values decrease with increasing thickness for the lowest frequency considered (1 Hz, red line) (Figure 8a), while in the hanging wall stations, the ccc values remain unaffected by changing the thickness of S-LVA (Figure 8b). This suggests that the footwall S-LVA has a very minor effect on the waveform changes observed in the hanging wall stations.

The effect of F-LVA is examined in Figure 9, where the 0.2 km thick F-LVA generates relatively little change in ccc on both the footwall and hanging wall sides. With increasing thickness from 1 to 5 km, the ccc reduces significantly for both the 1 and 2 Hz frequency bands, but the ccc remains unchanged in the 4 and 6 Hz energy bands. On the footwall side, the ccc changes for the lower frequency bands (1 and 2 Hz) are larger than in the higher frequency bands (4 and 6 Hz). On the hanging wall side, this only occurs when reaching a 5 km thickness of LVA. For a given thickness of F-LVA, the low-frequency ccc is reduced more on the footwall side, which is likely because the wave energy propagates through the area affected by the velocity change, whereas in the hanging wall side, the differential wavefield is mostly a result of energy scattered off the volume where the material properties changed where higher-frequency energy might be involved.

As illustrated in Figures 8b and 9b, the ccc change in the hanging wall side is only sensitive to F-LVA. To produce a comparable pattern with observation at the hanging wall in Figure 3b, a 1 km thick F-LVA is needed. The ccc reduction on the footwall side, however, is sensitive to both F-LVA and S-LVA as shown in Figures 8a and 9a. To fit the observed pattern on the footwall side in Figure 3a where large ccc reduction is similar over much of the frequency ranges, a 5 km thick S-LVA or 1 km thick F-LVA alone is required.

In order to better constrain the thickness of S-LVA, we further carry out a series of frequency dependency models using a combined effect of S-LVA and F-LVA with a fixed F-LVA thickness (1 km). On the hanging wall, the initial ccc drop (ccc < 0.7) occurs at 1.8 s after *S* arrival for lowest frequency band, whereas higher frequency occurs soon after the *P* and *S* arrivals (within 1 s) (Figure 10b). This pattern remains similar to Figure 9b for the various thickness of S-LVA considered. On the footwall side, the drop in *P* wave coda ccc for the 2 and 4 Hz frequency bands only appears when the S-LVA is introduced, as indicated by arrows in Figure 10a that is seen in Figure 8a but not in Figure 9a with F-LVA effect alone. This suggests that the 2 and 4 Hz ccc variation in *P* coda is sensitive to the thickness of S-LVA. This may be due to the fact that the S-LVA is located underneath the footwall stations, parallel to the wave propagation direction, whereas in the hanging

Figure 10. A combined model using a fixed 1 km thick F-LVA and S-LVA with changing thickness from 0.2 km to 5 km. The velocity reduction for both F-LVA and S-LVA is assumed to be −4%. The change of waveform similarity at different frequency bands is shown at (a) footwall station B and (b) hanging wall station D. (c) Cross section showing location of target stations and the combined model considering both surface low velocity anomaly and deep fault zone low velocity anomaly (grey area).

©2015. American Geophysical Union. All Rights Reserved.

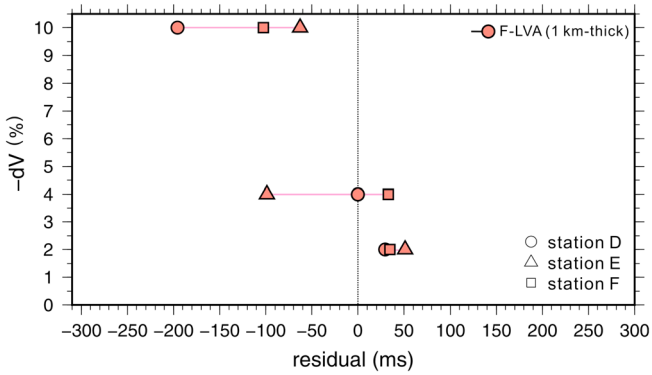

Figure 11. The effect of F-LVA at the hanging wall stations by F-LVA velocity reduction as a function of time residual assuming F-LVA thickness as 1 km. No S-LVA is assumed in this model. The residuals are the simulated minus the observed delay times. Simulated time lapse is determined by the maximum value in 5 s following the *S* arrival for different velocity reduction (−2%, −4%, and −10%). While increasing velocity reduction (d*V*) in the LVA, the delay time increases, and thus the residual becomes more negative. Horizontal lines indicate the residual from the same model but at three different stations.

wall stations, the differential wavefield is mostly from scattered energy bouncing off the F-LVA volume to arrive late in *S* coda. The comparison between footwall simulation (Figure 10a) and observation (Figure 3a) indicates that the S-LVA might be rather thin, around 1 km. But there is not enough sensitivity in the frequency dependency pattern to resolve the thickness of S-LVA.

3.3. Change in Path Effect: Strength of Low Velocity Anomaly

With the fixed 1 km thickness for F-LVA, we next examine the magnitude of the velocity reduction (d*V*) which explains the change in the delay time of the RES caused by the F-LVA. In Figure 11 the maximum value of the delay time is measured in a 5 s time window after the *S* arrival for different velocity reduction (−2%, −4%, and −10%) and plotted as "residual." The residual is determined by subtracting the simulated delay time from the observed delay time at hanging wall stations with epicentral distances of (station D) 75.1 km, (station E) 65.6 km, and (station F) 43.5 km, respectively (for station location, please see the cross section in Figure 10c). We find that the delay time increases with increasing velocity reduction (d*V*) in the LVA; therefore, residual becomes more negative (Figure 11). The −2% to −4% d*V* models appear to produce delay times that are comparable to that measured in the hanging wall stations (residual near 0).

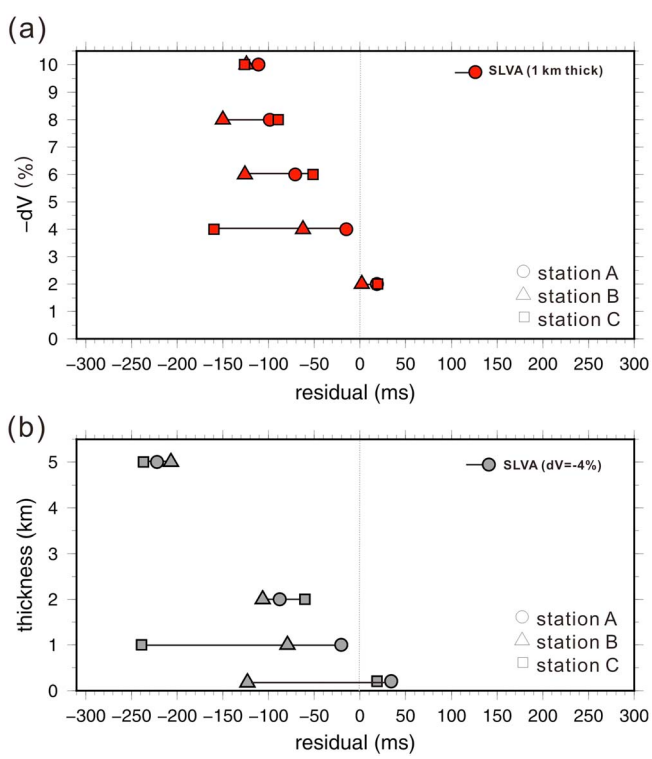

Figure 12. The effect of S-LVA at the footwall stations by S-LVA thickness and velocity reduction as a function of time residual. No F-LVA is assumed in this model. (a) Velocity reduction as a function of residual assuming S-LVA has 1 km thickness. Horizontal lines indicate the residual from the same model but at three different stations. (b) Thickness as a function of residual assuming S-LVA has d*V* = −4%.

The effect of S-LVA at the footwall stations is also examined in Figure 12, where the simulated delay times are compared with the observations by changing d*V* and thickness of S-LVA. Compared with the observations, greater delay times at footwall stations A–C are seen with increasing d*V* (Figure 12a) and thickness (Figure 12b) of the S-LVA alone. The best combination that gives residuals close to 0 for the three stations is a 1 km thickness with −2% d*V* S-LVA (red circles in Figure 12a) or a 0.2–1 km thickness with −4% d*V* (grey circles in Figure 12b).

A 1 km thick F-LVA zone with −4% d*V* is most consistent with our observations (Figures 11 and 12), so it is now introduced in a combined model where both F-LVA and S-LVA are considered

©2015. American Geophysical Union. All Rights Reserved.

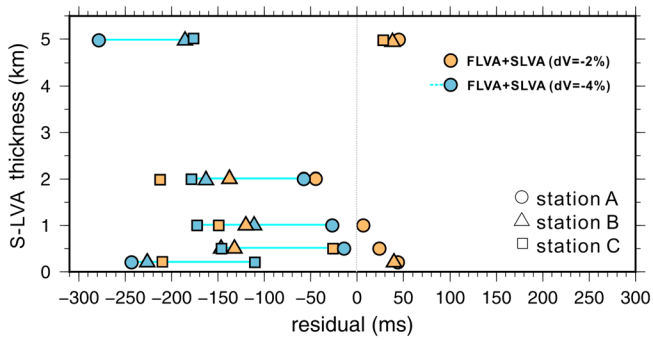

Figure 13. The effect of a combined model S-LVA at the footwall stations by S-LVA thickness and velocity reduction as a function of time residual. Thickness as a function of residual assuming a 1 km thick, −4% F-LVA with a −2% S-LVA (orange) and a −4% S-LVA (blue).

(Figure 13). Compared with −2% d*V* model, the −4% d*V* for S-LVA that illustrates negative residual over a wide range of thickness, therefore, is less likely. In the −2% d*V* S-LVA, a proper thickness of S-LVA appears to be ~0.5 km as indicated by orange symbols closer to residual = 0 at thickness = 0.5 km in Figure 13.

To conclude, to produce more delay times comparable to those observed in the hanging wall stations (stations D, E, and F), a velocity reduction of 2–4% in a 1 km thick F-LVA is needed. A combined model of F-LVA and S-LVA with −2% d*V* and thickness of 0.5 km is more likely, however, because the S-LVA is required to predict delay times comparable to those observed in the footwall stations (stations A, B, and C).

4. Discussion

4.1. Mechanism of Low Velocity Anomaly Following the Chi-Chi Earthquake

Comparing the observations with the synthesized wavefield, we find that fault zone damage explains the wavefield changes seen at the hanging wall stations. The combined effect of fault zone damage and near-surface damage is required to explain our observations in the footwall. The combined damage of the near surface and the fault zone makes the observed velocity changes 2–3 times larger at the footwall stations than the hanging wall stations. This can be seen in Figure 4, where the path-averaged velocity reduction for the first post-Chi-Chi repeating events in different RES is measured as 1–7.6% and <2% at the <110 km footwall and hanging wall stations, respectively.

After large earthquakes, the area near the rupture is often a region of concentrated damage. Highly fractured materials, changes in temperature, water saturation, and stress conditions all can play a role in reducing seismic wave velocities [*Poupinet et al.*, 1984; *Li et al.*, 1994; *Peng et al.*, 2003; *Rubinstein and Beroza*, 2007]. The velocity reduction induced by coseismic damage of rocks during dynamic rupture in a main shock is generally a few percent and have been widely studied through trapped waves [e.g., *Li et al.*, 1994, 2004, 2006], repeating earthquakes [e.g., *Peng et al.*, 2003; *Ben-Zion et al.*, 2003; *Schaff and Beroza*, 2004; *Peng and Ben-Zion*, 2006], seismic interferometry [*Sleep*, 2009], and ambient noise [*Wegler and Sens-Schönfelder*, 2007; *Wegler et al.*, 2009; *K. H. Chen et al.*, 2010; *J. H. Chen et al.*, 2010; *Hobiger et al.*, 2012; *Minato et al.*, 2012]. For example, the shear wave velocity is measured to be reduced by ~1.0–1.5% in a ~200 m wide zone after the 2004 Parkfield *M*6 event [*Li et al.*, 2006], ~2% in a ~120 m Wenchuan fault zone after a *M*5.5 aftershock event [*Yang et al.*, 2014]; and 1.5% after the *M*9.0 Tohoku-oki earthquake [*Minato et al.*, 2012].

The historical ruptures could happen along the same fault zone, such cumulative effect produces greater velocity reduction up to 20–60% compared with the surrounding rocks [e.g., *Li et al.*, 1998, 2000; *Vidale and Li*, 2003; *Cochran et al.*, 2009]. For example, using fault zone trapped waves, a 100–200 m wide low-velocity layer with 20–40% shear wave velocity reduction on the San Andreas fault was proposed by *Li et al.* [1997, 2004] and *Korneev et al.* [2003], and interferometric synthetic aperture radar and trapped waves revealed a 1.5 km wide zone along the Calico fault with 40–50% velocity reduction [*Cochran et al.*, 2009].

The width of faults, however, has widely varying definitions. Field observations indicate that the fault core is a narrow and localized slip zone (<50 cm wide) containing highly strained materials (e.g., breccias, cataclasites, and gouge) that accommodate most of the displacement [e.g., *Caine et al.*, 1996; *Chester et al.*, 1993]. There is also a damage zone around the fault core that has high permeability, which decreases with distance from the fault core. Using data collected from different works, *Savage and Brodsky* [2011] found that the fault zone width scales with fault displacement up to ~150 m. The width of damage zone, in general, is defined as the region where the fracture density is greater than the background value. Under

©2015. American Geophysical Union. All Rights Reserved.

such definition, the width of fault zone is often in a range of several tens to hundreds of meters [*Chester and Logan*, 1986; *Chester et al*., 1993; *Beach et al*., 1999; *Knott et al*., 1996; *Berg and Skar*, 2005; *Davatzes et al*., 2003; *Sagy and Brodsky*, 2009].

In this study, the repeating earthquakes that sample the fault zone properties before and after the main shock provide information on the coseismic change in seismic velocity, while the velocity contrast of the fault zone rocks with country rocks was not considered. Including a long-term damage zone affects the differential wavefield but does not substantively affect our conclusions (see Text S3 in the supporting information). We validate this by computing synthetics with a starting model embedded by velocity reduction up to 20% compared with the surrounding rocks. Including a damage zone in the starting model does not affect the timing of when the phase delays arrive but does affect their amplitude. Therefore, we do not consider the long-term damage because the spatial extent and amplitude of the velocity reduction of the long-term damage zone (produced by past ruptures) are not known. If there is a historical rupture-induced low-velocity layer, the earthquake-induced damage is likely larger than that suggested by our simulations. In addition, in order to generate greater damage of F-LVA ($-2 \sim -4\%$, 1 km thick) compared with S-LVA (-2%, 0.5 km thick) inferred from this study, we cannot rule out the role of the long-term fault zone damage. That is, the low-velocity fault zone due to the past earthquake ruptures could be further damaged by the Chi-Chi earthquake, while the near-surface materials were less affected.

We find the coseismic damage zone of the Chelungpu fault to be an approximately one kilometer thick region within which the velocities were reduced by 2% soon following the Chi-Chi rupture in 1999. The extent of the fault zone low-velocity layer likely highlights the section of the fault where the large motions took place at depth, producing a sudden and dramatic change in medium properties. Most of the Chi-Chi aftershocks, however, are located outside this localized rupture zone (east dipping Chelungpu fault) from near surface to 30 km at depth [*Chang et al*., 2000]. The deformation was likely much larger in the rupture zone than the area of aftershocks such that the area of the aftershocks did not experience a significant averaged velocity reduction.

Strong shaking induced velocity change is also likely. Near-surface damage, changes in fluid saturation, changes in crack density (crack opening and closing), and permeability changes can all produce near-surface velocity changes [*Poupinet et al*., 1984; *Schaff and Beroza*, 2004; *Rubinstein and Beroza*, 2004]. After the 2011 *M*9.0 Tohoku earthquake in Japan, a reduction in shear wave velocity is measured to be 5% in the upper few hundred meters [*Nakata and Snieder*, 2011]. Here the spatial extent of near-surface damage at footwall stations ($>$2% velocity reduction in Figure 4 at stations NSY, WNT, WGK, and TCU) coincides with geological site classes D and E—stiff and soft soils [*Lee et al*., 2001], primarily deformed and fractured sedimentary rocks. We believe this damage is concentrated in a ~0.5 km thick layer with a -2% velocity reduction induced by the earthquake. On the hanging wall, however, stations are mostly placed in hard rock (site B: shear wave velocity = 0.76 ~ 1.5 km/s), where the strong shaking may not be easily penetrated through connected fractures to greater depth for fluid flow. This is probably why there exists no clear evidence for significant velocity reduction at shallow surface on hanging wall. This also agrees with earlier observations that show that softer materials are more likely to be damaged by strong shaking than harder materials [*Rubinstein and Beroza*, 2004].

4.2. Healing Process Measured From Repeating Earthquakes

We can also assess how quickly the fault zone damage and coupling strength heals between earthquakes. This is of fundamental importance to understanding the earthquake cycle. As shown in Figure 14, the velocity reduction recovers with a rate of ~0.4% per year in the footwall side for all stations showing velocity reduction, whereas the recovery rate in the hanging wall is $<$0.2% per year. This means that the thinner near-surface damage (0.5 km thick, -2% dV) reflected from footwall stations is characterized by a healing rate twice that of the fault zone damage (1 km thick, $-2 \sim -4\%$ dV) revealed from hanging wall stations. This difference in healing rates suggests that the healing process is different for near-surface and fault zone damage.

The worldwide studies of near-surface damage inferred from repeating earthquakes indicate that crustal property changes following a large earthquake is restricted to several hundred meters in the crust with a recovery times of several years [*Baisch and Bokelmann*, 2001; *Ikuta et al*., 2002; *Schaff and Beroza*, 2004; *Rubinstein and Beroza*, 2004, 2005; *Li et al*., 2006; *Peng and Ben-Zion*, 2006]. The observed recovery time of several years is consistent with lab experiments predicted by healing of cracks [*Hiramatsu et al*., 2005],

©2015. American Geophysical Union. All Rights Reserved.

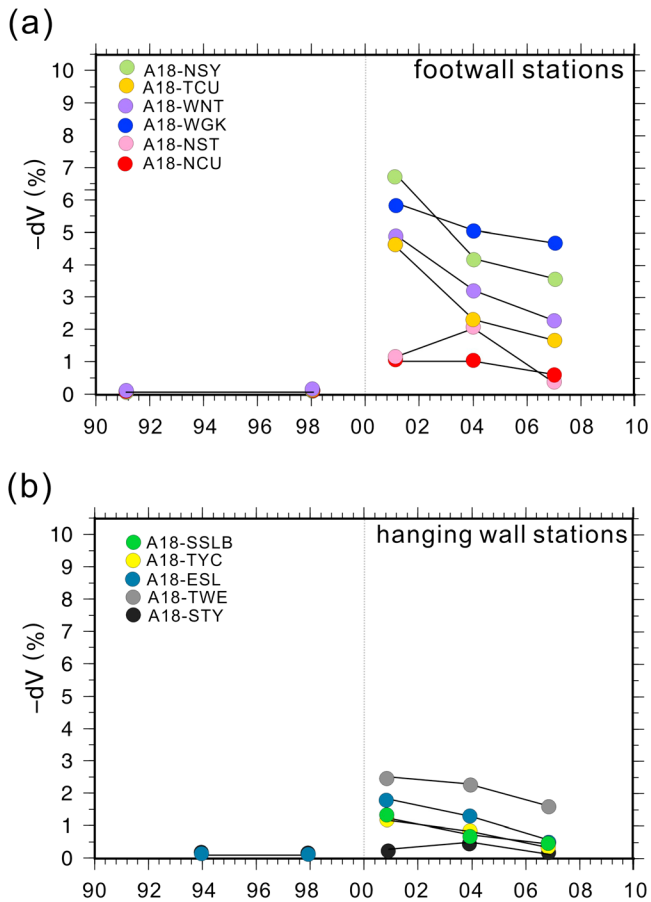

Figure 14. The observed recovery of velocity change at the (a) footwall and (b) hanging wall stations. Here only the stations that have high signal-to-noise ratio waveforms for all three post-Chi-Chi events are plotted.

suggesting that changes in the density of cracks and in water saturation (permeability of soil) may play important roles in surface damage [*Ishihara*, 1996; *Pavlenko and Irikura*, 2006; *Snieder and van den Beukel*, 2004]. In the damage rheology model, the healing of microcracks is more favored at high confining pressure, high temperature, and low shear stress [*Lyakhovsky et al.*, 1997].

Our work contrasts with numerical simulations of long-term crustal deformation by *Finzi et al.* [2011], which show that localized fault damage along the active fault cores (strike-slip fault) may rapidly heal at depth, while distributed off-fault damage at the shallow depth is more sustained over time. Dynamic rupture propagation model predicts a wider damage at the shallow depth with slower healing rate; at deeper part the damage is more localized with faster healing rate, assuming cracks opening and closing as the same mechanisms for coseismic and postseismic damage [*Ma*, 2008]. However, in the thrust system ruptured during the Chi-Chi earthquake, a higher healing rate for surface damage is observed, which cannot be explained by the depth-dependent crack healing behavior. We argue that in a deep fault zone, recovery from the material change due to movement of fault and/or fluid flow occurs more slowly. Another possibility is that the large number of aftershocks near the rupture zone (with 8–14 years relaxation time [*Loevenbruck et al.*, 2004]) may redamage the crust and perturb the healing of existing cracks, which could play a role in the slower healing rate observed on the hanging wall.

Direct observations of repeating earthquakes and simulations in this study provide important information for the magnitude and recovery of the coseismic near-surface damage versus fault zone damage. It takes longer for earthquake fault zones to recover the strength during the interseismic period, whereas the near-surface damage heals more quickly.

5. Summary

Remarkable changes in the waveform character of repeating earthquakes after the 1999 *M*7.6 Chi-Chi earthquake reveal the spatiotemporal extent of subsequent damage associated with the Chi-Chi event ~70 km away. While the character of waveform changes are consistent within the hanging wall and the footwall, the behavior of these changes is distinct on both sides of the fault. We observe both decreases in waveform similarity and delayed arrivals of phases (mainly in *S* wave coda). The waveform similarity reduction (ccc $<$ 0.7) and major waveform delays ($>$50 ms) arrive near/before the *S* wave arrival at the footwall stations but arrive in late *S* wave coda at the hanging wall stations. The ccc reduction remains similar over much of the range of frequencies considered (2–6 Hz) at the hanging wall stations, but at the hanging wall stations the most significant ccc reduction occurs for the highest frequencies considered. We also found that the velocity changes inferred are greater in the footwall stations (2.7–7.6%), than the $<$2% shear wave velocity change at hanging wall stations.

©2015. American Geophysical Union. All Rights Reserved.

To discriminate the effect of near-surface damage from fault zone damage, we calculated the postseismic changes in wavefield using a 2-D FDM for seismic wave simulation. We found that the change of seismic characteristics at hanging wall stations is sensitive to the effect of fault zone damage (low velocity anomaly), whereas the footwall stations are sensitive to both fault zone damage and near-surface damage. Deep fault zone damage from 8–19 km at depth and 30 km long near-surface damage on footwall side are necessary to explain the changes in the seismograms. In order to produce the observed frequency dependency behavior and delayed time measurements, damage zones, defined as the area where velocity reductions occurred, of approximately 1 km thick for the deep fault zone and 0.5 km thick for near-surface damage are needed. The velocity reductions in the fault zone damage and at the near surface are $-2 \sim -4\%$ and -2%, respectively. The near-surface damage may be characterized by a faster healing rate than fault zone damage, as revealed from the ongoing reduction in phase delays in the post-1999 events.

We note that the structural anomalies out of the 2-D plane are not taken into account by our wavefield simulations; thus, the estimated thickness and strength of the velocity anomalies might be overestimated. Future 3-D modeling is needed to obtain more quantitative estimates of near-surface and fault zone damage.

Acknowledgments
We thank Joan Gomberg, Elizabeth Cochran, Shu-Huei Hung, Wen-Tzong Liang, and Bill Ellsworthfor useful comments. We also thank the reviewers and the Editor Robert Nowack for their suggestions that improved this manuscript. Assistance in data collection and processing by Shu-Li Chen and Cheng-En Lin is greatly appreciated. This work was supported by Taiwan MOST grant MOST 103-2116-M-003 -001 -MY5. Seismic data are archived at the Central Weather Bureau Seismic Network (CWBSN) in Taiwan and Broadband Array in Taiwan for Seismology (BATS) operated by Institute of Earth Sciences, Academia Sinica.

References

Baisch, S., and G. H. Bokelmann (2001), Seismic waveform attributes before and after the Loma Prieta earthquake: Scattering change near the earthquake and temporal recovery, *J. Geophys. Res.*, *106*, 16,323–16,338, doi:10.1029/2001JB000151.

Beach, A., A. I. Welbon, P. J. Brockbank, and J. E. McCallum (1999), Reservoir damage around faults: Outcrop examples from the Suez rift, *Pet. Geosci.*, *5*(2), 109–116, doi:10.1144/petgeo.5.2.109.

Becker, J. J., et al. (2009), Global bathymetry and elevation data at 30 arc seconds resolution: SRTM30_PLUS, *Mar. Geod.*, *32*(4), 355–371.

Ben-Zion, Y., Z. Peng, D. Okaya, L. Seeber, J. G. Armbruster, N. Ozer, A. J. Michael, S. Baris, and M. Aktar (2003), A shallow fault-zone structure illuminated by trapped waves in the Karadere-Duzce branch of the North Anatolian fault, western Turkey, *Geophys. J. Int.*, *152*, 699–717.

Berg, S. S., and T. Skar (2005), Controls on damage zone asymmetry of a normal fault zone: Outcrop analyses of a segment of the Moab fault, SE Utah, *J. Struct. Geol.*, *27*, 1803–1822, doi:10.1016/j.jsg.2005.04.012.

Caine, J. S., J. P. Evans, and C. B. Forster (1996), Fault zone architecture and permeability structure, *Geology*, *24*, 1025–1028.

Chang, C. H., Y. M. Wu, T. C. Shin, and C. Y. Wang (2000), Relocation of the 1999 Chi-Chi earthquake in Taiwan, *TAO*, *11*(3), 581–590.

Chen, C. H., W. H. Wang, and L. L. Teng (2001), 3D velocity structure around the source area of the 1999 Chi-Chi, Taiwan, earthquake: Before and after the mainshock, *Bull. Seismol. Soc. Am.*, *91*(5), 1013–1027, doi:10.1785/0120000747.

Chen, J. H., B. Froment, Q. Y. Liu, and M. Campillo (2010), Distribution of seismic wave speed changes associated with the 12 May 2008 *Mw* 7.9 Wenchuan earthquake, *Geophys. Res. Lett.*, *37*, L18302, doi:10.1029/2010GL044582.

Chen, K. H., R. M. Nadeau, and R. J. Rau (2008), Characteristic repeating microearthquakes on an arc-continent collision boundary—The Chihshang fault of eastern Taiwan, *Earth Planet. Sci. Lett.*, *276*, 262–272, doi:10.1016/j.epsl.2008.09.021.

Chen, K. H., R. Bürgmann, R. M. Nadeau, T. Chen, and N. Lapusta (2010), Postseismic variations in seismic moment and recurrence interval of repeating earthquakes, *Earth Planet. Sci. Lett.*, *299*, 118–125.

Chen, K. H., T. Furumura, J. Rubinstein, and R. J. Rau (2011), Observations of changes in waveform character induced by the 1999 *Mw*7.6 Chi-Chi earthquake, *Geophys. Res. Lett.*, *38*, L23302, doi:10.1029/2011GL049841.

Chen, Y. G., W. S. Chen, J. C. Lee, Y. H. Lee, C. T. Lee, H. C. Chang, and C. H. Lo (2001), Surface rupture of 1999 Chi-Chi earthquake yields insights on active tectonics of Central Taiwan, *Bull. Seismol. Soc. Am.*, *91*(5), 977–985, doi:10.1785/0120000721.

Chester, F. M., and J. M. Logan (1986), Implications of mechanical properties of brittle faults from observations of the Punchbowl Fault Zone, California, *Pure Appl. Geophys.*, *124*, 79–106, doi:10.1007/BF00875720.

Chester, F. M., J. P. Evans, and R. L. Biegel (1993), Internal structure and weakening mechanisms of the San Andreas, *J. Geophys. Res.*, *98*, 771–786, doi:10.1029/92JB01866.

Cochran, E. S., Y. G. Li, P. M. Shearer, S. Barbot, Y. Fialko, and J. E. Vidale (2009), Seismic and geodetic evidence for extensive, long-lived fault damage zones, *Geology*, *37*(4), 315–318.

Davatzes, N. C., A. Aydin, and P. Eichhubl (2003), Overprinting faulting mechanisms during the development of multiple fault sets in sandstone, Chimney Rock fault array, Utah, USA, *Tectonophsics*, *363*, 1–18, doi:10.1016/S0040-1951(02)00647-9.

Finzi, Y., E. H. Hearn, V. Lyakhovsky, and L. Gross (2011), Fault-zone healing effectiveness and the structural evolution of strike-slip fault system, *Geophys. J. Int.*, *186*(3), 963–970.

Hiramatsu, Y., H. Honma, A. Saiga, and M. Furumoto (2005), Seismologcal evidence on characteristic time of crack healing in the shallow crust, *Geophys. Res. Lett.*, *32*, L09304, doi:10.1029/2005GL022657.

Hobiger, M., U. Wegler, K. Shiomi, and H. Nakahara (2012), Coseismic and postseismic elastic wave velocity variations caused by the 2008 Iwate-Miyagi Nairiku earthquake, Japan, *J. Geophys. Res.*, *117*, B09313, doi:10.1029/2012JB009402.

Hsu, Y. J., N. Bechor, P. Segall, S. B. Yu, L. C. Kuo, and K. F. Ma (2002), Rapid afterslip following the 1999 Chi-Chi, Taiwan earthquake, *J. Geophys. Res.*, *29*(16), 1754, doi:10.1029/2002GL014967.

Ikuta, R., K. Yamaoka, K. Miyakawa, T. Kunitomo, and M. Kumazawa (2002), Continuous monitoring of propagation velocity of seismic wave using ACROSS, *Geophys. Res. Lett.*, *29*(13), 1627, doi:10.1029/2001GL013974.

Ishihara, K. (1996), *Soil Behavior in Earthquake Geotechnics*, 1st ed., 350 pp., Clarendon Press, Oxford.

Ji, C., D. V. Helmberger, T. R. A. Song, K. F. Ma, and D. J. Wald (2001), Slip distribution and tectonic implication of the 1999 Chi-Chi, Taiwan earthquake, *Geophys. Res. Lett.*, *28*, 4379–4382, doi:10.1029/2001GL013225.

Kao, H., and W. P. Chen (2000), The Chi-Chi earthquake sequence: Active, out-of-sequence thrust faulting in Taiwan, *Science*, *288*, 2346–2349.

Kennett, B. L. N., and T. Furumura (2008), Stochastic waveguide in the Lithosphere: Indonesian subduction zone to Australian Craton, *Geophys. J. Int.*, *172*, 363–382.

Kim, K. H., J. M. Chiu, J. Pujol, K. C. Chen, B. S. Huang, Y. H. Yeh, and P. Shen (2005), Three-dimensional VP and VS structural model associated with the active subduction and collision tectonics in the Taiwan region, *Geophys. J. Int.*, *162*, 204–220.

©2015. American Geophysical Union. All Rights Reserved.

Knott, S. D., A. Beach, P. J. Brockbank, J. L. Brown, J. E. McCallum, and A. I. Welbon (1996), Spatial and mechanical controls on normal fault populations, *J. Struct. Geol.*, *18*(2–3), 359–372, doi:10.1016/S0191-8141(96)80056-3.

Korneev, V. A., R. M. Nadeau, and T. V. McEvilly (2003), Seismological studies at Parkfield IX: Fault-zone imaging using guided wave attenuation, *Bull. Seismol. Soc. Am.*, *80*, 1245–1271.

Kuo-Chen, H., F. Wu, and S. W. Roecker (2012), Three-dimensional *P* velocity structures of the lithosphere beneath Taiwan from the analysis of TAIGER and related seismic data sets, *J. Geophys. Res.*, *117*, B06306, doi:10.1029/2011JB009108.

Lee, C. T., C. T. Cheng, C. W. Liao, and Y. B. Tsai (2001), Site classification of Taiwan free-field strong-motion stations, *Bull. Seismol. Soc. Am.*, *91*, 1283–1297.

Lee, Y. H., Y. C. Chen, C. L. Chen, R. J. Rau, H. C. Chen, W. Lo, and K. C. Cheng (2006), Revealing surface deformation of the 1999 Chi-Chi earthquake using high-density cadastral control points in the Taichung area, central Taiwan, *Bull. Seismol. Soc. Am.*, *96*(6), 2431–2440, doi:10.1785/0120060055.

Li, Y. G., K. Aki, D. Adams, A. Hasemi, and W. H. K. Lee (1994), Seismic guided waves trapped in the fault zone of the Landers, California, earthquake of 1992, *J. Geophys. Res.*, *99*, 11,705–11,722, doi:10.1029/94JB00464.

Li, Y. G., W. Ellsworth, C. Thurber, P. Malin, and K. Aki (1997), Observations of fault-zone trapped waves excited by explosions at the San Andreas fault California, *Bull. Seismol. Soc. Am.*, *87*, 210–221.

Li, Y. G., J. E. Vidale, K. Aki, F. Xu, and T. Burdette (1998), Evidence of shallow fault zone strengthening after the 1992 *M*7.5 Landers, California, earthquake, *Science*, *279*, 217–219.

Li, Y. G., J. E. Vidale, K. Aki, and F. Xu (2000), Depth-dependent structure of the Landers fault zone from trapped waves generated by aftershocks, *J. Geophys. Res.*, *105*, 6237–6254, doi:10.1029/1999JB900449.

Li, Y. G., J. E. Vidale, and S. E. Cochran (2004), Low-velocity damaged structure on the San Andreas fault at Parkfield from fault-zone trapped waves, *Geophys. Res. Lett.*, *31*, L12S06, doi:10.1029/2003GL019044.

Li, Y. G., P. Chen, E. S. Cochran, J. E. Vidale, and T. Burdette (2006), Seismic evidence for rock damage and healing on the San Andreas fault associated with the 2004 *M* 6.0 Parkfield earthquake, *Bull. Seismol. Soc. Am.*, *96*(4B), 349–363.

Loevenbruck, A., R. Cattin, X. L. Pichon, S. Dominguez, and R. Michel (2004), Coseismic slip resolution and post-seismic relaxation time of the 1999 Chi-Chi, Taiwan, earthquake as constrained by geological observations, geodetic measurements and seismicity, *Geophys. J. Int.*, *158*, 310–326, doi:10.1111/j.1365-246X.2004.02285.x.

Lyakhovsky, V., Z. Reches, R. Weinberger, and T. E. Scott (1997), Non-linear elastic behavior of damaged rocks, *Geophys. J. Int.*, *130*, 157–166.

Ma, K. F., C. T. Lee, Y. B. Tsai, T. C. Shin, and J. Mori (1999), The Chi-Chi, Taiwan earthquake: Large surface displacements on an inland thrust fault, *Eos Trans. AGU*, *80*, 605–611, doi:10.1029/99EO00405.

Ma, K. F., J. Mori, S. J. Lee, and S. B. Yu (2001), Spatial and temporal slip distribution of the Chi-Chi, Taiwan, earthquake from strong motion, teleseismic and GPS data, *Bull. Seismol. Soc. Am.*, *91*, 1069–1087.

Ma, S. (2008), A physical model for widespread near-surface and fault zone damage induced by earthquakes, *Geochem., Geophys., Geosyst.*, *9*, Q11009, doi:10.1029/2008GC002231.

Marone, C., J. E. Vidale, and W. L. Ellsworth (1995), Fault healing inferred from time dependent variations in source properties of repeating earthquakes, *Geophys. Res. Lett.*, *22*, 3095–3098, doi:10.1029/95GL03076.

Minato, S., T. Tsuji, S. Ohmi, and T. Matsuoka (2012), Monitoring seismic velocity change caused by the 2011 Tohoku-oki earthquake using ambient noise records, *Geophys. Res. Lett.*, *39*, L09309, doi:10.1029/2012GL051405.

Nakata, N., and R. Snieder (2011), Near-surface weakening in Japan after the 2011 Tokoku-Oki earthquake, *Geophys. Res. Lett.*, *38*, L17302, doi:10.1029/2011GL048800.

Pavlenko, O., and K. Irikura (2006), Nonlinear behavior of soils revealed from the records of the 2000 Tottori, Japan, earthquake at stations of the digital strong-motion network Kik-Net, *Bull. Seismol. Soc. Am.*, *96*(6), 2131–2145, doi:10.1785/0120060069.

Peng, Z., and Y. Ben-Zion (2006), Temporal changes of shallow seismic velocity around the Karadere-Düzce branch of the North Anatolian Fault and strong ground motion, *Pure Appl. Geophys.*, *163*, 567–600, doi:10.1007/s00024-005-0034.

Peng, Z., Y. Ben-Zion, A. J. Michael, and L. Zhu (2003), Quantitative analysis of seismic trapped waves in the rupture zone of the 1992 Landers, California earthquakes: Evidence for a shallow trapping structure, *Geophys. J. Int.*, *155*, 1021–1041, doi:10.1111/j.1365-246X.2003.02109.x.

Peng, Z., J. E. Vidale, C. Marone, and A. Rubin (2005), Systematic variations in recurrence interval and moment of repeating aftershocks, *J. Geophys. Res.*, *32*, L15301, doi:10.1029/2005GL022626.

Perfettini, H., and J. Avouac (2004), Postseismic relaxation driven by brittle creep: A possible mechanism to reconcile geodetic measurements and the decay rate of aftershocks, application to the Chi-Chi earthquake, Taiwan, *J. Geophys. Res.*, *109*, B02304, doi:10.1029/2003JB002488.

Poupinet, G., W. L. Ellsworth, and J. Frechet (1984), Monitoring velocity variations in the crust using earthquake doublets: An application to the Calaveras Fault California, *J. Geophys. Res.*, *89*, 5719–5731, doi:10.1029/JB089iB07p05719.

Rubinstein, J. L., and G. C. Beroza (2004), Evidence for widespread nonlinear strong ground motion in the *Mw* 6.9 Loma Prieta earthquake, *Bull. Seismol. Soc. Am.*, *94*, 1595–1608.

Rubinstein, J. L., and G. C. Beroza (2005), Depth constraints on nonlinear strong ground motion from the 2004 Parkfield earthquake, *Geophys. Res. Lett.*, *32*, L14313, doi:10.1029/2005GL023189.

Rubinstein, J. L., and G. C. Beroza (2007), Full waveform earthquake location: Application to seismic streaks on the Calaveras Fault, California, *J. Geophys. Res.*, *112*, B05303, doi:10.1029/2006JB004463.

Sagy, A., and E. E. Brodsky (2009), Geometric and rheological asperities in an exposed fault zone, *J. Geophys. Res.*, *114*, B02301, doi:10.1029/2008JB005701.

Savage, H. M., and E. E. Brodsky (2011), Collateral damage: Evolution with displacement of fracture distribution and secondary fault strands in fault damage zones, *J. Geophys. Res.*, *116*, B3405, doi:10.1029/2010JB007665.

Schaff, D. P., and G. C. Beroza (2004), Coseismic and postseismic velocity changes measured by repeating earthquakes, *J. Geophys. Res.*, *109*, B10302, doi:10.1029/2004JB003011.

Schaff, D. P., G. C. Beroza, and B. E. Shaw (1998), Postseismic response of repeating aftershocks, *Geophys. Res. Lett.*, *25*(24), 4549–4552, doi:10.1029/1998GL900192.

Sleep, N. H. (2009), Depth of rock damage from strong seismic ground motions near the 2004 Parkfield mainshock, *Bull. Seismol. Soc. Am.*, *99*(5), 3067–3076.

Snieder, R., and A. van den Beukel (2004), The liquefaction cycle and the role of drainage in liquefaction, *Granular Matter*, *6*, 1–9, doi:10.1007/s10035-003-0151-9.

Vidale, J., and Y. G. Li (2003), Damage to the shallow Landers fault from the nearby Hector Mine earthquake, *Nature*, *421*, 524–526.

Vidale, J. E., W. L. Ellsworth, A. Cole, and C. Marone (1994), Rupture variation with recurrence interval in eighteen cycles of a small earthquake, *Nature*, *368*, 624–626.

©2015. American Geophysical Union. All Rights Reserved.

Wegler, U., and C. Sens-Schönfelder (2007), Fault zone monitoring with passive image interferometry, *Geophys. J. Int.*, *168*, 1029–1033.
Wegler, U., H. Nakahara, M. Korn, and K. Shiomi (2009), Sudden drop of seismic velocity after the 2004 *Mw* 6.6 Mid-Niigata earthquake, Japan, observed with passive image interferometry, *J. Geophys. Res.*, *114*, B06305, doi:10.1029/2008JB005869.
Yang, W., H. Ge, B. Wang, J. Hu, S. Yuan, and S. Qiao (2014), Active source monitoring at the Wenchuan fault zone: Coseismic velocity change associated with aftershock event and its implication, *Earthquake Sci.*, *27*(6), 599–606.
Yu, S. B., et al. (2001), Preseismic deformation and coseismic displacements associated with the 1999 Chi-Chi, Taiwan, earthquake, *Bull. Seismol. Soc. Am.*, *91*, 995–1012.
Zeng, Y., and C. H. Chen (2001), Fault rupture process of the 20 September 1999 Chi-Chi, Taiwan, earthquake, *Bull. Seismol. Soc. Am.*, *91*, 1088–1098.

©2015. American Geophysical Union. All Rights Reserved.